MeV-scale Physics in MicroBooNE

MICROBOONE-NOTE 1076-PUB

The MicroBooNE Collaboration

Abstract: The scope of this public note is to present preliminary measurements of MeV energy signatures and relevant backgrounds for beam neutrino interactions using a dedicated reconstruction technique, expanding upon the original study by ArgoNeuT. We also use this technique to identify and quantitatively analyze the low energy activity emanating from the field cage support ribs in the MicroBooNE detector and discuss how the usage of similar construction materials could be a source of background for low energy physics analyses in future neutrino detectors such as the Deep Underground Neutrino Experiment (DUNE). We also highlight the application of the low energy reconstruction technique to studies of neutrino interactions from core-collapse supernovae and muons decaying at rest (μDAR).

1. Introduction

This public note presents the first evaluation of both position and energy reconstruction of sub-MeV energy depositions from neutrino interactions in the MicroBooNE Liquid Argon Time Projection Chamber (LArTPC) utilizing unblinded datasets from parts of Run 1 (October 15, 2015 - October 15, 2016) and Run 3 (October 27, 2017 - September 17, 2018). Developing the capability to study these low-energy depositions is necessary for several LArTPC physics analyses envisioned for MicroBooNE, as well as DUNE and other LArTPC experiments. These analyses include: supernova neutrino searches; ^{39}Ar studies; reconstruction of nuclear de-excitations and neutron scatters in neutrino interactions and neutron captures on Ar.

This note is organized as follows. Section 2 introduces the MeV-scale reconstruction and its implementation in MicroBooNE. Section 3 highlights the measurement of the cosmogenic backgrounds that mimic the low energy activity of interest. In Section 4 we discuss the MeV-scale energy signatures produced in Booster Neutrino Beam (BNB) neutrino interactions within the detector. In Section 5 we present the spatial distribution of reconstructed low-energy activity within the detector, that reveals unexpected 'hot-spot' regions within the detector which are correlated to physical objects present in the detector volume. We also investigate the radiological origin of the hot-spot activity and arrive at preliminary conclusions. Finally in Section 6 we describe the applications of the low energy activity analysis in developing the reconstruction for ν_e events originating from muon decay at rest (μDAR) and core-collapse supernovae.

email: MICROBOONE_INFO@fnal.gov

2. MeV-scale Activity Reconstruction

MicroBooNE primarily studies accelerator neutrino events with energies in the range of 0.2-2.0 GeV. The

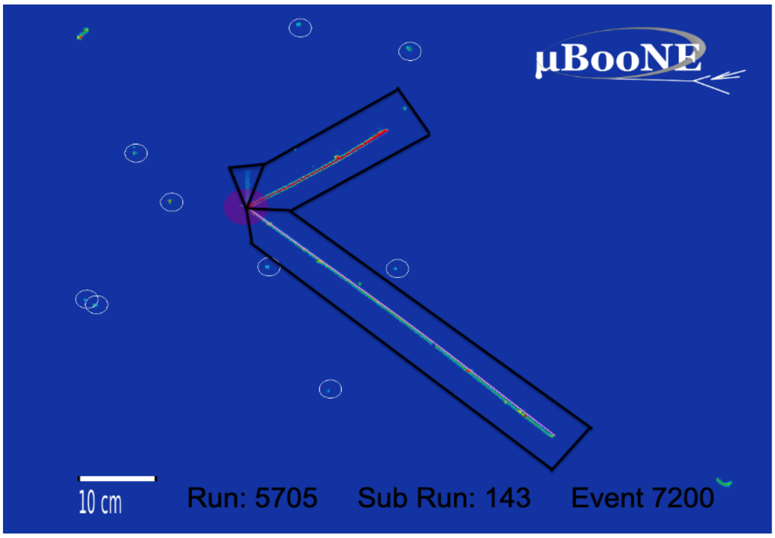

Figure 1: MeV-scale electromagnetic activity reconstructed around the neutrino vertex (On-beam data) in the form of white circles around hits. The neutrino vertex is indicated by the pink circle. Neutrino correlated tracks are enclosed by conical and cylindrical veto region of radius 5cm, whereas cosmogenic tracks are enclosed by a cylinder of radius 15cm

analysis described in this note focuses on the study of isolated energy depositions in the detector that have energies of the order 0-5 MeV. Such depositions can originate from nuclear de-excitation gamma rays, neutron scatters, and radiological activity, such as ^{39}Ar beta decays. Fig. 1 illustrates an example of a neutrino interaction in the MicroBooNE detector, where the encircled objects are low-energy charge depositions that have been reconstructed using the tools developed in this analysis.

ArgoNeuT has successfully demonstrated the reconstruction of low-energy MeV photons from nuclear de-excitations and neutron scatters in neutrino interactions, and this analysis adapts that same approach [1]. Given that MicroBooNE is a much larger detector with finer wire pitch (3 mm) than ArgoNeuT (4 mm), it is possible to reconstruct low-energy objects much further away from the interaction vertex and with better spatial resolution. In addition, lower intrinsic noise due to the use of cold electronics in MicroBooNE detector allows for lower energy thresholds, which enhances the reconstruction of extremely low energy electromagnetic interactions.

MeV-energy photons can be produced in neutrino-argon interactions due to the de-excitation of the target nucleus and the inelastic scattering of final-state particles. When a neutrino interacts with an ^{40}Ar nucleus, the remaining residual nucleus is often left in an excited state, which de-excites via the emission of a photon or a cascade of photons with energies ranging up to $\sim$ 10 MeV. Final-state particles, such as neutrons, inelastically scatter off other ^{40}Ar nuclei or are captured to produce photons in the same energy range. Photons are neutral particles and hence cannot be directly detected. Instead we detect electrons resulting from a photon interaction, which, in liquid argon (LAr) over the energy range of 0-10 MeV is predominantly Compton scattering [2]. Photons generally lose only a small fraction of their total energy in each Compton scattering interaction, leading to a spray of small and scattered energy deposits associated to each photon.

2.1. Lowering Energy Thresholds

For an MeV-scale reconstruction, it is necessary to lower hit finding thresholds from the default values to be

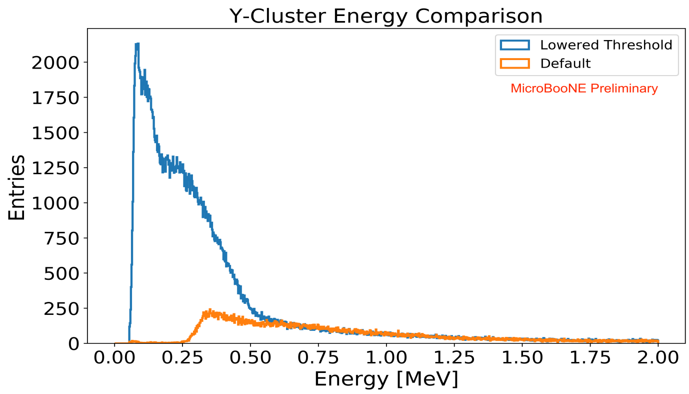

Figure 2: Reconstructed energy spectra of low and high threshold data samples

able to recover as much energy as possible. Thresholds are primarily set at the signal processing stage of data analysis. The main objective behind all threshold lowering exercises is to identify the noise floor and to vary threshold parameters so that any energy deposition above that floor can be reconstructed. There are four main parameters which enable threshold lowering in data : Nσ formation on collection plane, Nσ formation on the induction planes (where Nσ refers to the number of standard deviations above from the root mean squared (RMS) noise thresholds on each wire plane), Region of Interest (ROI) amplitude in the number of electrons (peak value for a single hit) and ROI average in the number of electrons (mean value for a single hit). In the default threshold data set, the respective values for Nσ formation on collection and induction plane, ROI amplitude in the number of electrons and ROI average in the number of electrons are 3,5,1000 and 500, whereas that in low threshold data set are 2,3,300 and 100 respectively.

In Fig. 2, we see the comparison of the energy spectra between the data sample with default thresholds and the one with lowered thresholds. In the default threshold dataset, we are able to reconstruct activity as low as 0.25 MeV in energy, whereas in the low threshold dataset, the energy reconstruction can be as low as 0.1 MeV. Additionally, in the low threshold dataset we see indications of contributions from noise and ^{39}Ar activity in the 0-0.5 MeV energy range.

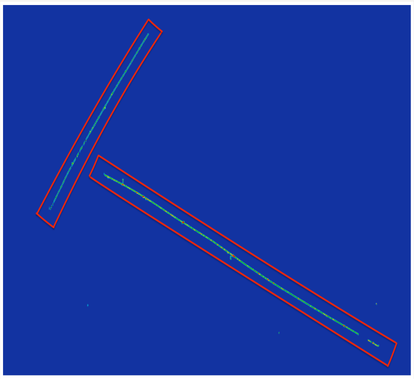

(a) Cosmogenic tracks are enclosed within cylindrical exclusion zones of radius 15 cm

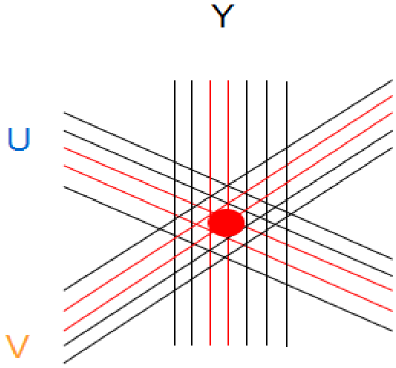

(b) Plane Matching of a cluster is established by checking the drift time and wire overlap between the collection and the two induction planes.

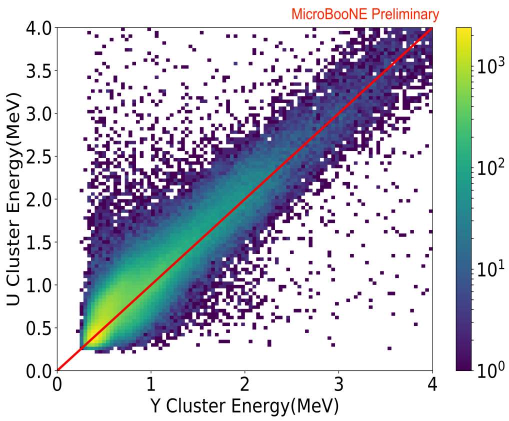

(c) Good energy agreement between Y-Plane clusters and their matched counterparts on the U-Plane

Figure 3: Schematic showing (a) the cosmic activity removal, (b) 3-D plane matching and (c) energy reconstruction as the three stages of the MeV-scale reconstruction in MicroBooNE

2.2. Cosmic Activity Removal

MicroBooNE's surface location exposes the detector to significant cosmic ray activity that can potentially mimic beam-related interactions. The main challenge for the MeV-scale reconstruction is the low energy activity associated with cosmic muon tracks, such as δ-rays and bremsstrahlung photons, that is present in the vicinity of the cosmic muon tracks. This activity is present mainly in the form of single hits on wires. The drift coordinate (x) obtained for the hit is assumed to be in time with the beam and is determined by its drift time. The beam direction coordinate (z), on the other hand, is determined by the wire number on the collection plane. This analysis only considers low energy electromagnetic activity that falls outside of a 15 cm 2-D rectangle around each cosmic track identified by the Pandora multi algorithm automated pattern recognition [3], as seen in Fig. 3(a). This ensures that only the electromagnetic activity that is uncorrelated to the cosmic tracks survives to the next analysis stage. Assuming that there are about 19 cosmological tracks per event, each of size 0.2m$\times$2m in two dimensions, we lose about 7.6m^2 (28.6%) of the surface area due to the rectangular cuts.

2.3. Plane Matching

The low energy activity within the detector volume after cosmic track removal consists primarily of single hits. We achieve 3-D reconstruction by matching the drift times of clusters (group of hits) across the 3 wire planes. We begin by searching for the drift time overlap in the two induction planes for low energy activity lying on the collection plane. This ensures that random noise hits are removed as they are unlikely to find a match across multiple planes. Once a match for a hit is established, the intersection between the collection plane hit wire and the induction plane hit wire yields the y-coordinate, as shown in the schematic in Fig. 3(b). Since we obtain two independent values by plane matching with the two induction planes, false matches are eliminated by setting a difference tolerance of 1 cm between the two independent y-coordinate values. These 3-D plane matched clusters are henceforth referred to as spacepoints.

2.4. Energy Reconstruction

After having spatially reconstructed the 2-D clusters as spacepoints, the Analog to Digital Conversion (ADC) hit integral information associated with every spacepoint is obtained from the collection plane. Energy reconstruction for the spacepoints is done using the NIST [4] tables, which provide track lengths for electrons in LAr of energies from 10 keV to 1 GeV. To allow for energy reconstruction, the pulse area (ADC x time) of a spacepoint is converted into number of electrons by multiplying it with the appropriate electronic calibration factor, depending upon the plane from which the cluster was registered. The next step is to convert the collected charge into the original energy deposited during the ionization process using a fit function. This is the energy reconstruction approach used by the analysis in ArgoNeuT.

Once the energy reconstruction is applied to matched clusters, there is clear agreement between the energy of clusters matched on the induction plane to the energy of clusters on the collection plane, as seen in Fig. 3(c).

3. Measurement of cosmogenic and ambient beam-external backgrounds

One of the primary reasons cosmogenic backgrounds are a nuisance for the MicroBooNE detector is the slow drift time, which causes the accumulation of cosmogenic backgrounds. In each MicroBooNE event, there is an average of $\sim$ 19 cosmic tracks. The long cosmic muon tracks themselves don't pose the real challenge when it comes to reconstruction of MeV-scale activity in the detector, but it is the δ-rays and bremsstrahlung photons in their vicinity which mimic the signature of low energy electromagnetic activity from neutrinos. There are other even more problematic sources of background such as argon spallation products and cosmogenic neutrons which scatter off the argon nucleus. To be able to get a quantitative measurement of these backgrounds, we analyze Off-beam (BNB EXT) data. All events with electromagnetic showers are rejected for the analysis since showers produce a large number of single hit activity within the detector, quite often,in the vicinity of cosmogenic tracks which may make background estimation difficult.

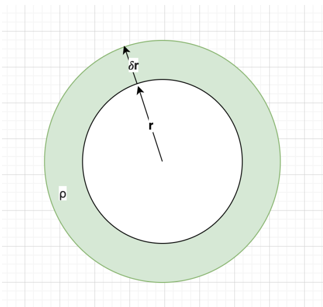

(a) An imaginary sphere of radius r with an incremental shell of radius δr around it

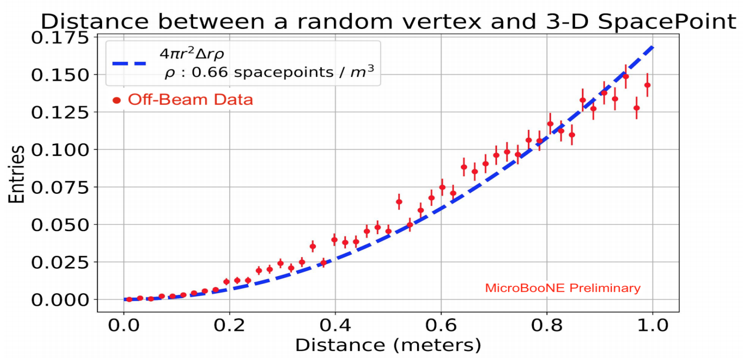

(b) A curve fit (blue) to the distance between a randomly generated vertex and spacepoint within the detector from Off-beam data (red)

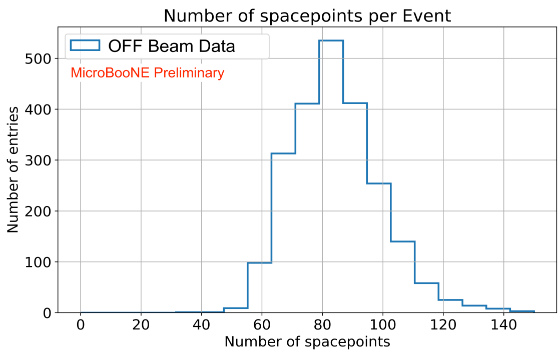

(c) Number of spacepoints per event from Run 1 Off-beam data

Figure 4: Data driven measurement for cosmogenic backgrounds.

In order to measure the rate of uniform cosmogenic backgrounds in the detector, we draw an imaginary sphere of radius r with an incremental shell of radius δr around a randomly chosen point in the TPC, as seen in Fig. 4(a). The idea is that the (background) spacepoints distribution around each randomly chosen point is a function of $r^2\delta r\rho$, where ρ is the density of the background spacepoints. Fig. 4(b) shows a plot of the distance between a randomly chosen point and spacepoints within the detector. The distance curve is plotted using data (red) and the $r^2\delta r\rho$ fit function is plotted in blue. The fit function yields a value of ρ= 0.66 spacepoints/m^3 which forms the preliminary measurement for the cosmogenic background spacepoints. The disagreement between the fit function and data could be explained by geometric effects. For instance, if the randomly chosen point were to lie close to the edge of the detector, imaginary sphere around it would be cut off by the detector boundary. A more realistic version of the model taking into account boundary effects is under development. As seen in the Fig. 4(c), the histogram showing the number of spacepoints from Off-beam Run 1 data peaks at 80 spacepoints per event. To put things in perspective, in atmospheric argon, ^{39}Ar beta decays occur at a rate of roughly one Becquerel per kilogram. A previous calculation [5] shows that at this rate and for a readout window of 4.8 ms (wider than the truncated waveform currently used, of 3.2ms duration), this rate corresponds to approximately 400 decays in the readout window, or roughly 7 decays/m^3 per event.

4. BNB Neutrino Interactions

Analysis of BNB (On-beam) data, BNB-EXT (Off-beam) data and Monte Carlo (MC) simulation samples allows us to make correlations between the neutrino vertex and the reconstructed spacepoints in terms of the number, the distance and energy of the spacepoints around the neutrino vertex. The neutrino vertex is identified using the Pandora multi-algorithm approach to automated pattern recognition of neutrino events.[3] Again, all events with electromagnetic showers are rejected to simplify signal reconstruction as shower activity may be reconstructed too close to the neutrino vertex. In addition, we use a cylindrical and conical exclusion of 5 cm to eliminate bremsstrahlung and δ-ray activity coming off the neutrino-correlated tracks as shown in Fig. 1. Conical veto on the tracks is aimed to reconstruct as much of the final state particles in vicinity of the neutrino interaction vertex as possible while also making sure that track correlated backgrounds are rejected.

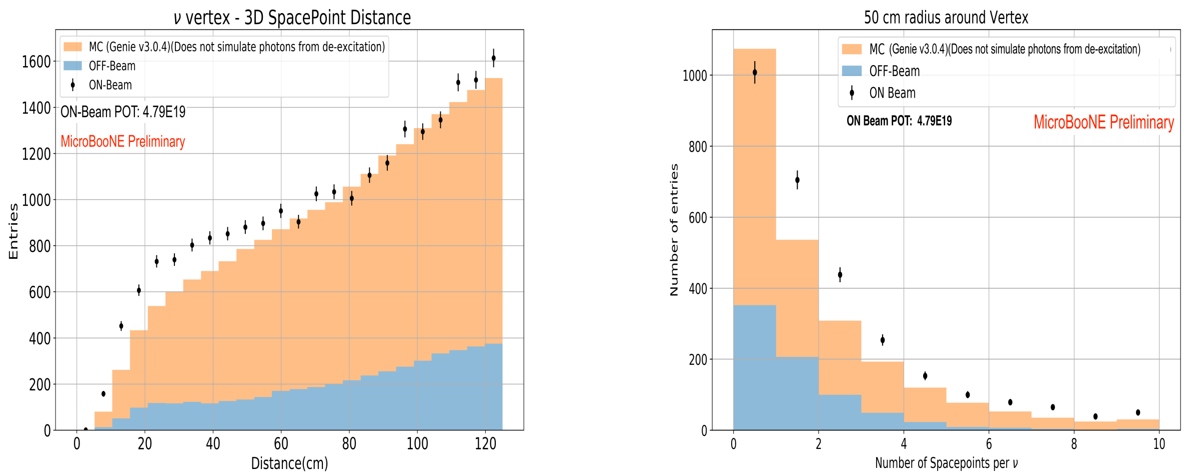

(a) Distance between a neutrino vertex and spacepoints

(b) Number of spacepoints around a neutrino vertex

Figure 5: Plots showing (a) an On-beam excess in the distance between neutrino vertex and reconstructed spacepoints up to 75 cm over Off-beam and MC simulation samples, and (b) Greater average number of spacepoints around the neutrino vertex in On-beam data as compared to Off-beam and MC simulation samples.

In Fig. 5, we present a comparison of On-beam, Off-beam and MC simulation Cosmic overlay samples in the form of stacked histograms. Overlay refers to the fact that the cosmic background in the MC sample is taken from data. On-beam data is shown in black with error bars, Off-beam is shown in blue, whereas MC overlay is shown in orange. In this comparison, both the Off-beam and MC overlay histograms have been normalized to the On-beam protons on target (POT). We see that for for Fig. 5(a), the MC overlay curve is larger than

Off-beam at distances up to 75 cm and for Fig. 5(b) for any number of spacepoints around the vertex. This is due to the fact that in Off-beam data set there are no low energy final state products such as de-excitation gamma rays or neutrons due to the absence of neutrino interactions. The only contribution in the Off-beam curve comes from cosmogenic and intrinsic radiological activity. In MC overlay, however, we have simulated final state neutrons coming from neutrino interactions on Ar, in addition to the contribution from intrinsic radiological activity and the cosmogenic activity coming from cosmic overlays. Again, in Fig. 5(a) for distances up to 75 cm around the neutrino vertex, there is an On-beam excess over both MC overlay and Off-beam curves owing to the fact that On-beam data includes de-excitation gamma rays from neutrino interactions which are missing in MC with overlays because GENIE v3.0.4 doesn't simulate them. For distances above 125 cm, the data and MC agreement needs to take into account the boundary effects of the detector and is being studied. In addition, On-beam data set has contribution from final state neutrons as well as cosmogenic activity. The average multiplicities of spacepoints in a 50 cm radius around the neutrino vertex for On-beam data, MC Overlays and Off-beam data are 1.95, 1.81 and 1.11, respectively, further corroborating the gap between data and MC simulation as seen in Fig. 5(b). It is to be noted that we do not correct for the different acceptance due to the absence of neutrino-correlated tracks that veto volume in the On-beam sample.

5. Distribution of spacepoints within the MicroBooNE detector

Once the low-energy depositions are plane matched, the spatial distribution of the reconstructed spacepoints within the detector volume is studied.

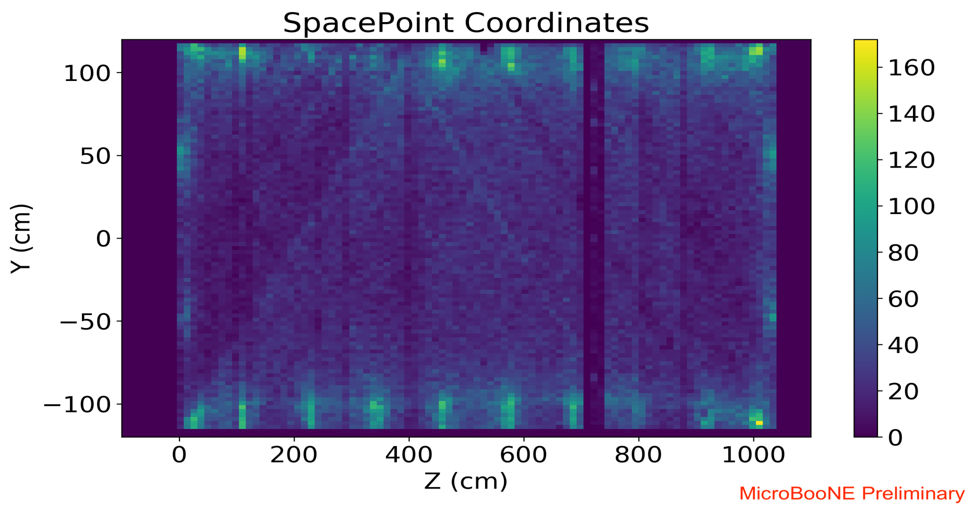

Figure 6: A 2-D plot showing the spacepoint distribution within the detector in the Y-Z plane, as seen in Off-beam data

Fig. 6 shows that the spacepoints are mostly uniformly distributed in the interior of the detector. The vertical bands near z = 400 cm and z = 700 cm correspond to the unresponsive channels in MicroBooNE readout. Such unresponsive channels can also be seen as much fainter bands at an angle of ±60° across the YZ spacepoint distribution plot in Fig. 6. The spatial distribution of spacepoints within the MicroBooNE detector in Off-beam shows small hot-spot regions (shown in green) in the YZ Plane as seen in Fig. 6.

This hot-spot activity also appears across MC simulation with cosmic overlay, across Off-beam and across On-beam as multiple vertical or horizontal bands. This hot-spot activity is clearly not present in the MC simulation sample with no data overlays, which confirms that this hot-spot activity is not known or simulated within the MC simulation.

5.1. Correlation of the hot-spot activity to the material sources present within the detector

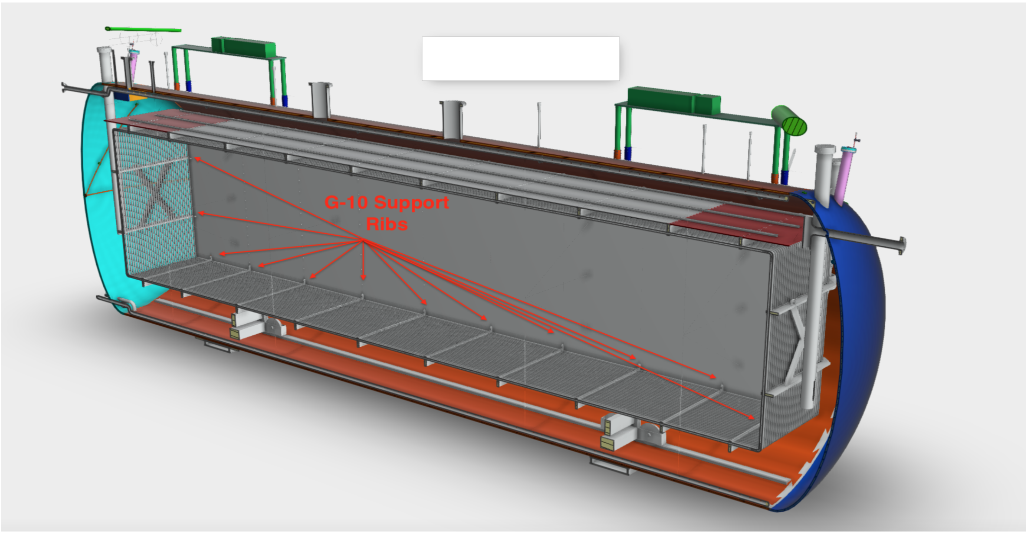

Figure 7: : Sliced CAD drawing of the MicroBooNE detector TPC showing the G-10 support ribs which are spatially coincident with the hot-spot regions, as seen in the spacepoint distribution plots.

We determined that the location of the hot-spot activity in the MicroBooNE detector coincides with the G-10 ribs that act as support for the field cage tubes. This can be verified from the MicroBooNE Computer Aided Design (CAD) drawing as seen in Fig. 7.

To investigate the origin of hot-spots around the G-10 support bars, we first isolate all reconstructed 3-D spacepoints found in the vicinity of the G-10 support beams. We then compare these G-10 hot-spot spacepoints with the spacepoints within the interior of the TPC. This comparison is shown in Fig. 8 and Fig. 9, respectively. This allows the analysis of the rate and energy distribution of the spacepoints from two different regions of the detector with seemingly different distributions. Note the different colorbar scales while comparing Fig. 8 and Fig. 9.

5.2. Rate of G-10 activity from Off-beam data

We first investigate the time dependence of the spacepoint distribution around the G-10 region, by comparing Off-beam data taken in 2016 (Run 1) to data taken during 2018 (Run 3). The idea is to try and see if there is

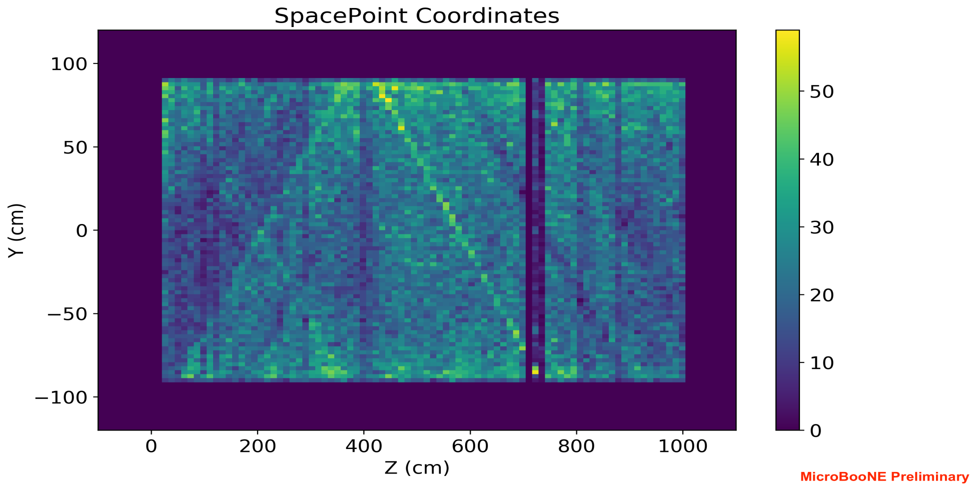

Figure 8: 2-D plot showing the distribution of spacepoints in the interior of the TPC.

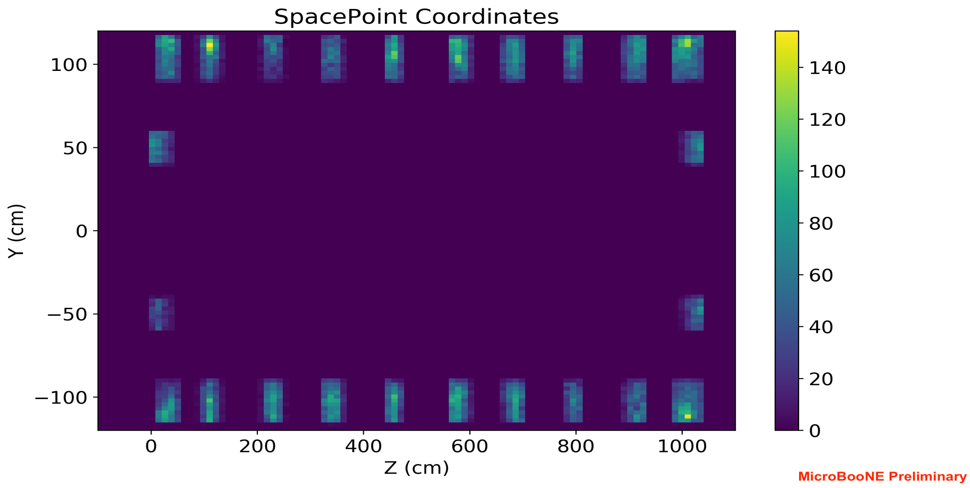

Figure 9: 2-D plot showing the distribution of spacepoints in the G-10 region only.

any time dependence of the activity.

As seen from the plots in Fig. 10, the activity is relatively flat between Run 1 and Run 3. More data points (different binning) on the two plots in Fig. 10 is due to the fact that there are more events in Run 1 Off-beam open dataset as compared to Run 3 Off-beam open dataset.

5.3. Comparison of the rates between top and bottom G-10 support bars

As seen in Fig. 11, the contribution to the hot-spot event rate is slightly more in the top as compared to the bottom G-10 support bars. This difference could be attributed to either one or both of the following:

Cosmogenic Activation: There is more cosmogenic interaction at the top of the detector as compared to the

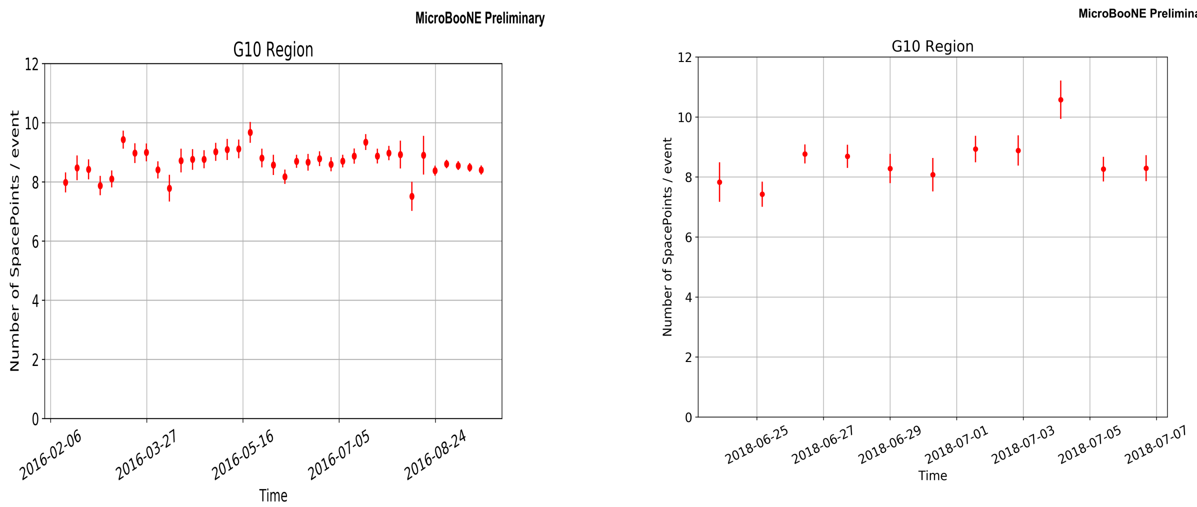

(a) Run 1

(b) Run 3

Figure 10: Number of spacepoints per event from the G-10 region over Run 1(left) and Run 3(right) of MicroBooNE

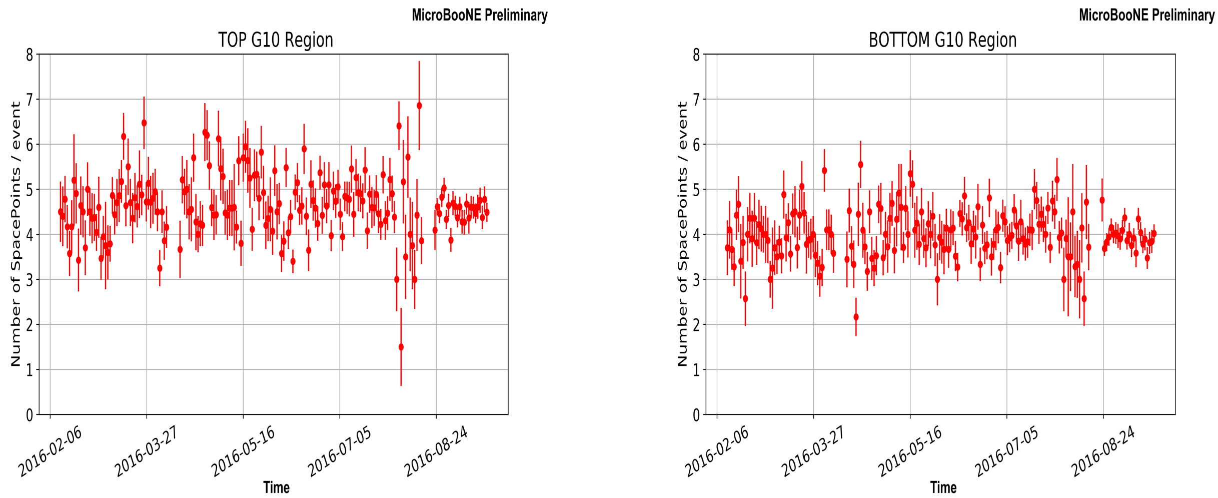

(a) Top

(b) Bottom

Figure 11: Comparison of the number of spacepoints per event in the top and bottom G-10 regions as seen in data

bottom since all the cosmogenic tracks do not go through the detector and might stop inside the detector. Additionally, this difference in hot-spot activity at the top and bottom could be attributed to neutron spallation attenuation/down-scattering of the primary cosmic neutron flux by the argon bulk.

Spacecharge Artifact: The space charge effect [6] is the build-up of slow-moving positive ions in a detector due to ionization from cosmic rays, leading to a distortion of the electric field within the detector. This effect leads to a displacement in the reconstructed position of signal ionization electrons in LArTPC detectors.

5.4. Composition of the G-10 Material

G-10 is a high pressure fiberglass laminate made by stacking multiple layers of glass cloth in epoxy resin mixture and compressed under heat until the epoxy cures. Electrical non conduction and good tensile strength make it the material of choice for manufacturing printed circuit boards and structural supports.[7]. G10 typically consists of 60% glass fiber and 40% epoxy.[8]. Glass fiber itself contains about 1% of Potassium dioxide (K_2O), which, in turn, is composed of about 83% natural potassium (K) by weight [9]. ^{40}K makes up 0.012% (120 ppm) of natural potassium. The half life of ^{40}K is about 1.25 x 10^9 years.

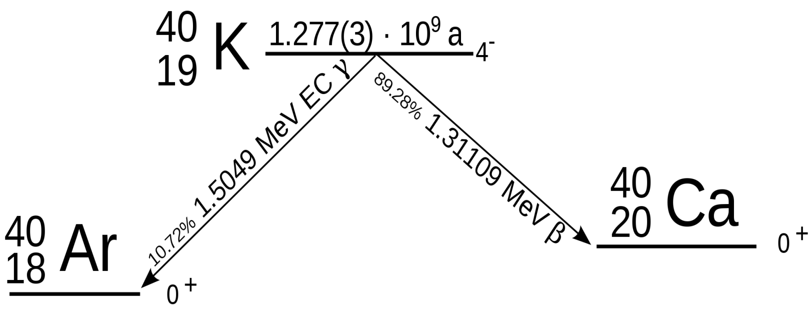

Figure 12: Decay Scheme for ^{40}K

^{40}K decays to ^{40}Ca about 89.28% of the time with emission of a beta particle (β^-, an electron) with a maximum energy of 1.31 MeV and an anti-neutrino. It can also decay to ^{40}Ar 10.72% of the time by electron capture (EC), with the emission of a neutrino and then a 1.46 MeV gamma ray.[10]

5.5. Theoretical calculation of the rate of G-10 activity

The mass of G-10 in field-cage support bars is 215.6 kg. That would mean the mass of natural potassium in the G-10 support bars is about 1.08 kg and hence the mass of ^{40}K in the G-10 bars is about 1.3×10^{-4} kg. Dividing this by the mass of ^{40}K atom (6.64x10^{-26} kg) yields the number of ^{40}K atoms in all of the G-10 material present in the MicroBooNE detector, which is approximately 2×10^{21} atoms.

We use the radioactive decay formula for our calculation: $R = N\left(\frac{0.693}{T_{\frac{1}{2}}}\right)$ where

N : Original Number of ^{40}K atoms

$\mathbf{T}_{\frac{1}{2}}$: Half life of ^{40}K

R : Rate of ^{40}K decay

Using this formula, where N=2×10^{21}, $T_{\frac{1}{2}}$=1.25×10^9 years= 3.94×10^{16} s, we calculate that R = 35000 decays/s.

Using references [7] [8] [9] and multiplying R by the MicroBooNE event readout window (3.2 ms) we arrive at a rate of ∼ 112 decays per event readout window coming from the G-10 material, which is significantly higher than the observed value of ∼ 8 decays per event. This difference has been discussed in Section 5.7

5.6. Energy Profile of the G-10 spacepoints

Using the energy reconstruction described in Section 2, we present the energy spectra for the G-10 spacepoints and for the spacepoints belonging to the rest of the detector. For this study we use a smaller sample of Off-beam data with lowered thresholds.

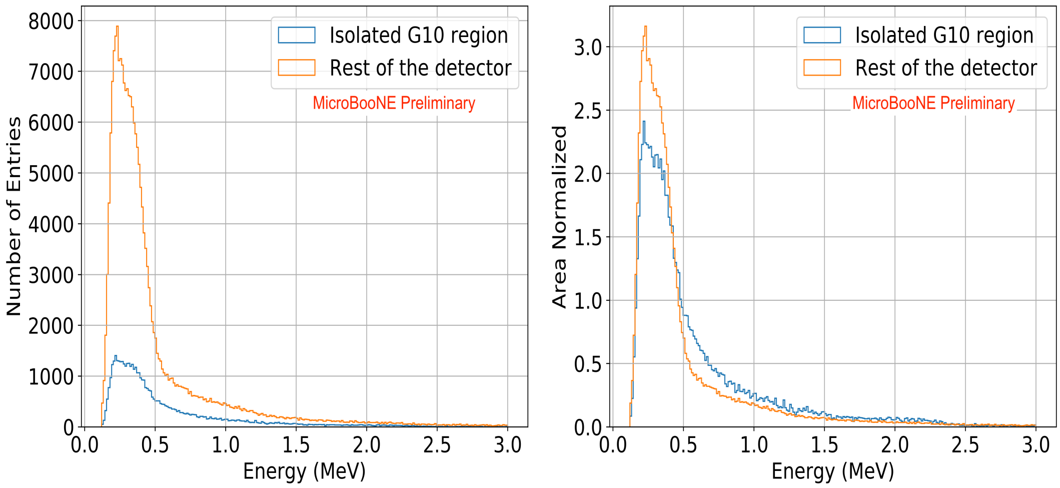

Figure 13: Absolute (left) and area normalized (right) comparison of energy spectra for spacepoints from the G-10 region and those from the rest of the detector.

As seen in Fig. 13, for the most part, the energy spectra of the two regions looks similar. This might indicate that the energy deposition from both the interior of the detector and the G-10 hotspots could come from the same kind of energy deposition, such as photons. However, more work needs to be done to conclusively establish that claim. To account for the fact that the energy spectrum of the G-10 region may have contamination from the activity in the rest of the detector, we take a difference of the two area scaled histograms in Fig. 14 (left) to arrive at a purely G-10 only energy spectrum. Here, area scaling is done, not by comparing the actual physical dimensions of the G-10 support ribs, but by comparing the area of the two different fiducial cuts for the interior of the TPC and the isolated G-10 hot spots as they appear in Fig. 8 and Fig. 9. The final energy spectrum for the G-10 material is shown in Fig. 14 (right).

5.7. Conclusions about the G-10 activity

- If the hypothesis that hot-spot activity in MicroBooNE is related to decays of radioactive contaminants in the G-10 material is true, then it is important to understand the difference between the different physical phenomena that contribute to the total decays. Any beta emission from the bulk of the G-10 is likely going to be reabsorbed within the G-10 material itself. Surface beta decays and gamma emissions from

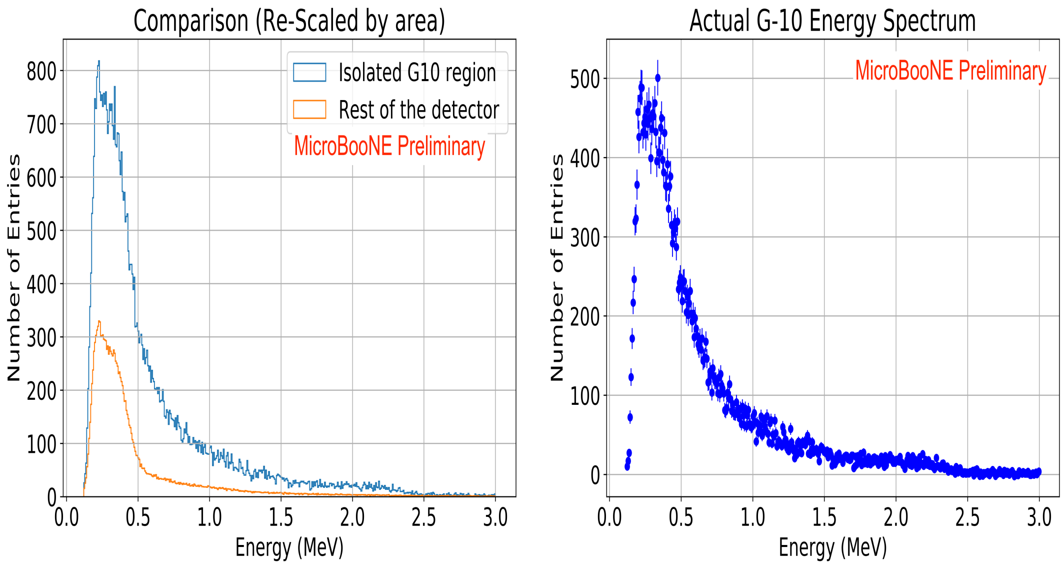

Figure 14: Left:Energy spectra comparison re-scaled by area of the hot spot regions, Right: The energy spectra of the G-10 spacepoints obtained by subtracting the two histograms on the left

the G-10, on the other hand, are more likely to be the main contribution that shows up as reconstructed activity.

- In addition to the fact that reconstruction efficiency for detecting all activity coming from the G-10 material is never going to be a full 100%, there is also some inefficiency that creeps in while trying to make a one to one correspondence between a radioactive decay and a reconstructed spacepoint. Further work needs to be done to connect ^{40}K decays per event to number of reconstructed spacepoints per event. Since a reconstructed spacepoint is build up of multiple hits, it could be possible that 1 reconstructed spacepoint corresponds to multiple decays from the G-10, or vice-versa, where multiple reconstructed spacepoints correspond to 1 radioactive decay.

- G-10 material is going to be used in future neutrino detectors such as the Deep Underground Neutrino Experiment. As an example, for a 10kt single phase module, there are going to be 150 Anode Plate Assemblies (APA) of size 6 m$\times$2.3 m and 300 Cathode Plate Assemblies (CPA) of size 1.2 m$\times$4 m using quite a significant amount of G-10 in the form of insulating panels, hanger plates, bushings and printed circuit boards (PCB). Activity from G-10 in DUNE could form considerable backgrounds, if it behaves similar to what we are observing in MicroBooNE and may require large fiducial volume cuts near the boundary of the TPC.

6. Application of MeV-scale Reconstruction

One of the primary applications of the MeV-scale analysis in MicroBooNE is to pave the way for reconstructing other neutrino interactions in a similar energy regime. The main candidates for such low energy reconstruction are muon decay-at-rest neutrino events and supernova neutrino events.

6.1. Muon Decay at Rest (μDAR) Neutrino Events

Accelerator neutrino beams are created via decay of hadrons in flight, primarily pions. As seen in the schematic

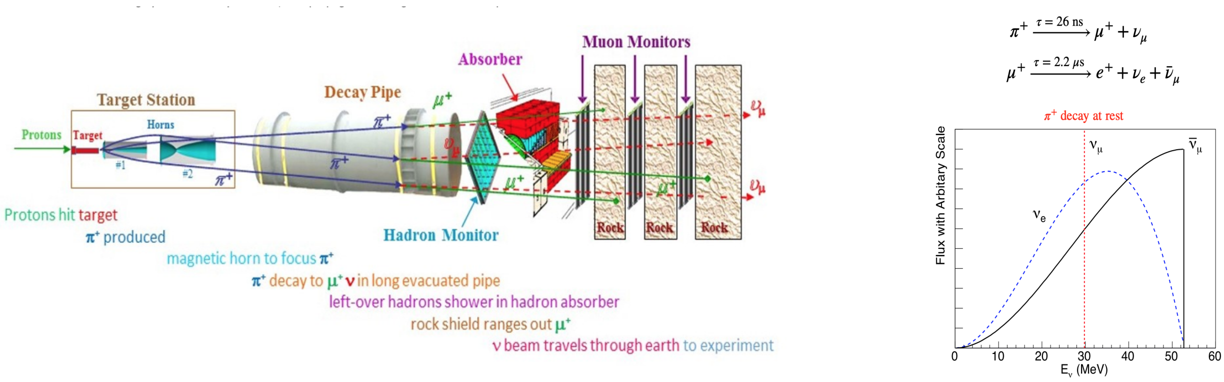

(a) NuMI Beam

(b) μDAR Neutrinos

Figure 15: Schematic showing (a) Neutrinos at the Main Injector beam line at Fermilab[11] (b) Electron Neutrino Production from Pion Decay[12]

in Fig. 15 (a), a focusing horn in the beam apparatus enables selection of mostly positive (negative) hadrons, leading to the production of mostly muon (anti)neutrinos. Muons from the beam will also decay and produce neutrinos. Some of these muons will stop before decaying, that is, they decay at rest. A recent simulation study [13] of the Fermilab Neutrinos at the Main Injector (NuMI) beam suggests that the NuMI μDAR neutrino flux is large enough for a measurement to be attempted. The black and dashed blue curves in Fig. 15 (b) show, respectively, the energy spectra of $\bar{\nu}_\mu$ and ν_e produced by μ^+ decay at rest. These spectra, which are accurately predicted by the standard model and well understood, lie in the tens-of-MeV regime and thus are suitable candidates to be studied using the MeV-scale reconstruction.

6.2. Supernova Neutrino Events

A massive star after having fused most of the lighter elements in the outer layers begins to fuse heavier elements at the core due to the inward pull of gravity. After entering the giant phase the core contracts enough to fuse Helium into Iron via Carbon, Oxygen, Neon and Silicon.[14] Unable to produce more heat in the core, gravity further compresses it until Iron atom hits degeneracy pressure. When degeneracy pressure yields to the inward pull of gravity, electrons combine with protons to give neutrons and neutrinos. About 99% of the star's gravitational binding energy is released in the form of tens-of-MeV neutrinos.

6.3. Model of Argon Reaction Low-Energy Yields (MARLEY)

MARLEY [15] is a Monte Carlo event generator that simulates tens-of-MeV neutrino-nucleus interactions. For the studies considered in this note, version 1.1.1 of MARLEY was used to simulate the charged-current process

$$\nu_e + {}^{40}\mathrm{A}r \longrightarrow e^- + {}^{40}\mathrm{K}^* \tag{1}$$

together with the subsequent de-excitations of the remnant ^{40}K nucleus. Scattering cross sections were computed using the configuration referred to as “dataset A” in ref. [15]. The default nuclear level and de-excitation γ-ray data, adapted for use in MARLEY from version 1.6 of the TALYS nuclear code [16], were also used in the simulations. The nuclear de-excitation products considered by MARLEY include γ-ray photons, nucleons, and composite nuclear fragments with mass number $A \leq 4$ (e.g., deuterons, alpha particles).

Two samples of MARLEY events were generated for this note using `uboonecode`, a MicroBooNE-specific software package that implements extensions to the LArSoft [17] framework. Incident neutrino energies were simulated for the first sample using the built-in μDAR ν_e spectrum implemented in MARLEY. The second sample used a time-integrated supernova ν_e spectrum based on the “GVKM” calculation described in ref. [18]. For simplicity, vertex positions for each neutrino event were sampled uniformly within the active volume of the MicroBooNE detector.

6.4. Reconstruction of Core Collapse Supernova and μDAR neutrino events

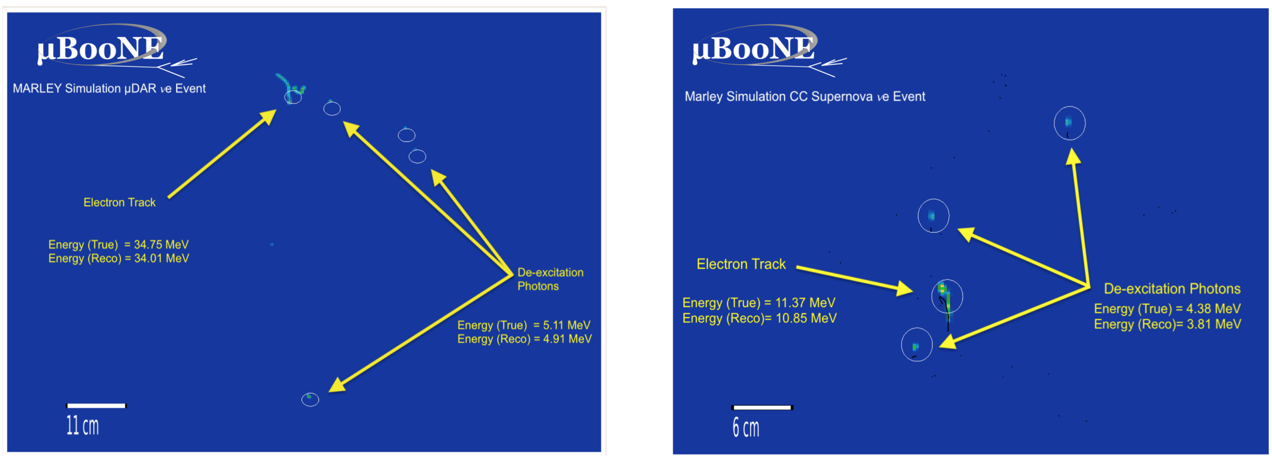

(a) μDAR event

(b) Supernova neutrino event

Figure 16: MicroBooNE detector collection plane event displays showing the spatial and energy reconstruction for the final state products from (a) μDAR Neutrino Event and (b) Supernova Neutrino Event

The MeV-scale reconstruction performs fairly well in terms of both spatial and energy reconstruction of the low energy de-excitation γ-rays produced in both μDAR and supernova neutrino events as seen in the

MicroBooNE detector collection plane event displays in Fig. 16. As seen in both event displays, the summed true and reconstructed energies for the de-excitation γ-rays agree with each other within a few hundred keV. It is worth noticing that even though the energy reconstruction for electron tracks is also promising, the spatial reconstruction of the short electron track is still a work in progress. This is primarily because the MeV-scale analysis focuses on reconstruction of clusters which are generally 2 hits in size, whereas an electron track for both μDAR and supernova neutrino events is on the order of 10–20 hits in size.

7. Summary and Conclusions

The MeV-scale analysis described in this note is the first in the LArTPC world to reach the 100 keV energy threshold in the reconstruction of low energy activity associated with neutrino interactions. Using this low energy reconstruction technique has allowed the observation and analysis of activity that appears associated with G-10 material within the MicroBooNE detector, highlighting a possible concern and background source when utilizing G-10 as a construction material in future LArTPCs such as DUNE. Further studies are planned to model the presence of radioactive materials in the MicroBooNE G-10 support bars, and to study their impact using these dedicated low energy reconstruction tools. This analysis also has relevance for future studies of supernova neutrino interactions in MicroBooNE and other LArTPCs, where the developed tools may improve the position reconstruction of the electron track from a charged current supernova neutrino event.

References

[1] ArgoNeuT collaboration, Demonstration of MeV-scale physics in liquid argon time projection chambers using ArgoNeuT, Phys. Rev. D **99** (2019) 012002 [1810.06502].

[2] A. H. Compton, A Quantum Theory of the Scattering of X-rays by Light Elements, Phys. Rev. **21** (1923) 483.

[3] MicroBooNE collaboration, The Pandora multi-algorithm approach to automated pattern recognition of cosmic-ray muon and neutrino events in the MicroBooNE detector, Eur. Phys. J. C **78** (2018) 82 [1708.03135].

[4] M. J. Berger, J. S. Coursey, M. A. Zucker and J. Chang, ESTAR, PSTAR, and ASTAR: Computer Programs for Calculating Stopping-Power and Range Tables for Electrons, Protons, and Helium Ions (version 1.2.3), 2005.

[5] "Study of Reconstructed ^{39}Ar Beta Decays at the MicroBooNE Detector." `https://microboone.fnal.gov/wp-content/uploads/MICROBOONE-NOTE-1050-PUB.pdf`.

[6] M. Mooney, The microboone experiment and the impact of space charge effects, arXiv (2015) [1511.01563].

[7] "NEMA Grade G-10 Glass Epoxy Laminate." `https://thegundcompany.com/wp-content/uploads/2016/11/NEMA-G10-EPGC-201-from-The-Gund-Co.pdf`.

[8] "ATOMIC AND NUCLEAR PROPERTIES OF MATERIALS (PDG)." `https://www-pdg.lbl.gov/2004/reviews/atomicrpp.pdf`.

[9] "SDD Materials : E-Glass fiberglass." `http://personalpages.to.infn.it/~tosello/EngMeet/ITSmat/SDD/E_glass.html`.

[10] "^{40}K Decay Scheme." `http://www.nucleide.org/DDEP_WG/Nuclides/40K_tables.pdf`.

[11] "NuMI Neutrino Beamline." `https://targets.fnal.gov/NuMI_neutrino_beam.html`.

[12] L. B. Auerbach, R. L. Burman, D. O. Caldwell, E. D. Church, J. B. Donahue, A. Fazely et al., Measurements of charged current reactions of ν_e on ^{12}C, Phys. Rev. C **64** (2001) 065501.

[13] C. Grant and B. R. Littlejohn, Opportunities With Decay-At-Rest Neutrinos From Decay-In-Flight Neutrino Beams, arXiv Preprint (2016) [1510.08431].

[14] A. Bueno, I. Gil-Botella and A. Rubbia, Supernova Neutrino Detection in a liquid Argon TPC, arXiv Preprint (2003) [hep-ph/0307222v1].

[15] S. Gardiner, Nuclear Effects in Neutrino Detection, Ph.D. thesis, University of California, Davis, 2018.

[16] A. J. Koning, S. Hilaire and M. C. Duijvestijn, TALYS-1.0, in Proceedings of the International Conference on Nuclear Data for Science and Technology, O. Bersillon, F. Gunsing, E. Bauge, R. Jacqmin and S. Leray, eds., pp. 211–214, EDP Sciences, 2008, DOI.

[17] E. Snider and G. Petrillo, LArSoft: toolkit for simulation, reconstruction and analysis of liquid argon TPC neutrino detectors, Journal of Physics: Conference Series **898** (2017) 042057.

[18] J. Gava, J. Kneller, C. Volpe and G. C. McLaughlin, Dynamical Collective Calculation of Supernova Neutrino Signals, Phys. Rev. Lett. **103** (2009) 071101.